



Cite this: *RSC Adv.*, 2023, 13, 20068

Electroless Ni plated nanostructured TiO₂ as a photocatalyst for solar hydrogen production†

Priyanka N. Birla, Sudhir Arbuj,  Manish D. Shinde, Shany Joseph, Sunit Rane, Sulabha Kulkarni and Bharat Kale *

Herein, we have demonstrated a facile electroless Ni coated nanostructured TiO₂ photocatalyst for the first time. More significantly the photocatalytic water splitting shows excellent performance for hydrogen production which is hitherto unattempted. The structural study exhibits majorly the anatase phase along with the minor rutile phase of TiO₂. Interestingly, electroless nickel deposited on the TiO₂ nanoparticles of size 20 nm shows a cubic structure with nanometer scale Ni coating (1–2 nm). XPS supports the existence of Ni without any oxygen impurity. The FTIR and Raman studies support the formation of TiO₂ phases without any other impurities. The optical study shows a red shift in the band gap due to optimum nickel loading. The emission spectra show variation in the intensity of the peaks with Ni concentration. The vacancy defects are pronounced in lower concentrations of Ni loading which shows the formation of a huge number of charge carriers. The electroless Ni loaded TiO₂ has been used as a photocatalyst for water splitting under solar light. The primary results manifest that the hydrogen evolution of electroless Ni plated TiO₂ is 3.5 times higher (1600 μmol g⁻¹ h⁻¹) than pristine TiO₂ (470 μmol g⁻¹ h⁻¹). As shown in the TEM images, nickel is completely electroless plated on the TiO₂ surface, which accelerates the fast transport of electrons to the surface. It suppresses the electron–hole recombination drastically which is responsible for higher hydrogen evolution using electroless Ni plated TiO₂. The recycling study exhibits a similar amount of hydrogen evolution at similar conditions which shows the stability of the Ni loaded sample. Interestingly, Ni powder loaded TiO₂ did not show any hydrogen evolution. Hence, the approach of electroless plating of nickel over the semiconductor surface will have potential as a good photocatalyst for hydrogen evolution.

Received 11th May 2023
Accepted 25th June 2023

DOI: 10.1039/d3ra03139j

rsc.li/rsc-advances

Introduction

The environment and energy have been progressively decisive issues in the last two decades, in connection with the elusive climatic changes emerging worldwide due to the vast use of fossil fuels. Thus, energy sources that are bountiful, regenerative, and free from carbon emissions are in sizable demand. Solar energy is securing a lot of attention as a sustainable and clean energy source. However, for the sake of its practical utilization, solar energy must be reconstructed into other types of energy, such as chemical fuels, electricity, heat, *etc.* which allow for more effective storage and conveyance. Among chemical fuels, hydrogen (H₂) is quintessentially ascribed to its highest energy capacity of 143 MJ kg⁻¹ among all materials over the globe and its emission-free superiority, generating water as the only by-product from combustion energy.¹ Predominantly for the production of hydrogen some cardinal energy systems

are implemented such as thermal, electrical, photonic and biochemical.^{2,3}

Considering the key energy systems, plenty of techniques were employed for the generation of hydrogen, some of them are conventional electrolysis,^{4–6} high-temperature electrolysis, thermochemical Cu–Cl, hybrid sulphur, Mg–Cl cycles, thermolysis, photoelectrolysis, photoelectrocatalysis, photo-electrochemical cells (PECs), photocatalysis,⁷ hybrid photocatalytic Cu–Cl cycles,⁸ and still search for finding a better technology is going on globally.

Among them, photocatalysis involving the storage of chemical energy in hydrogen molecule enabled by the solar energy is the most cost-effective way of hydrogen production having high efficiency and abundant resource of semiconductor materials such as oxides and sulphides.^{9,10}

Commercialisation of hydrogen production through water splitting has few limitations such as low solar conversion output, fractional solar radiation adsorption range and high rate of charge carrier recombination.^{11,12}

A dependable photocatalyst needs to fulfil important requisites like suitable band gap exhibiting efficient electron–hole separation and transport leading to surface catalytic proton

Centre for Materials for Electronics Technology (C-MET), Ministry of Electronics and Information Technology (MeitY), Panchavati, Pune 411008, India. E-mail: bbkale@cmet.gov.in

† Electronic supplementary information (ESI) available: XRD, SEM, TEM images and electrochemical tests. See DOI: <https://doi.org/10.1039/d3ra03139j>



reduction as well as water oxidation, and negligible photo-corrosion.¹² Homogeneous photocatalysts possessing these requirements are limited and hence heterogeneous photocatalyst with two or more distinct photocatalysts needs to be employed to overcome the above drawbacks enabling the industrial scale production.¹³

Majority of the semiconductor photocatalysts belong to transition metal cations consisting of metal sulfides, nitrides and oxides having d^0 and d^{10} configurations. Metal sulphide and nitride photocatalysts such as CoS_2 , MoS_2 , Ni_3S_2 , NiCoS_4 , CdS , $\text{In}_x\text{Ga}_{1-x}\text{N}$, GaN , Ta_3N_5 etc. are highly prone to photo-corrosion and consequently are chemically less stable.^{14–17}

Though, metal oxides such as ZnO , WO_3 , Nb_2O_5 , Ag_3PO_4 , Bi_2WO_6 , Ta_2O_5 , TiO_2 , etc. are the most explored materials as photocatalysts, resistance to chemical, thermal and photo-corrosion, easy availability, lower production cost and wide absorption range makes TiO_2 the material of choice since the time of Honda and Fujishima.^{18,19} Application of TiO_2 in solar-light-driven photocatalysis has been limited owing to its wide bandgap of 3.2 eV which lies in the ultraviolet (UV) region comprising of only 4% of solar spectrum.

Various approaches have been ventured to overcome the drawbacks associated with TiO_2 such as doping (for example with transition metal cations like Cr^{3+} , Fe^{2+} , Ni^{2+} and Rh^{3+} , etc.)^{20,21} and use of noble metals (Pt ,^{22,23} Pd , Rh ,^{24,25} Ag and Au ^{26,27}) and transition metals like Ni , Cu , Zn , Mn , etc. as co-catalysts.^{11,28,29}

For noble metals, cost is the hindering factor in their practical use as co-catalyst. In recent years, the transition metals like Ni-based (NiO ,³⁰ Ni_2P ,³¹ NiS ,³² and NiSe_2 (ref. 33)), Cu-based ($\text{Cu}(\text{OH})_2$,³⁴ CuO ³⁵), and Co-based (CoO ,³⁶ Co_3O_4 (ref. 37)) co-catalysts have received considerable attention in the photocatalytic field, attributable to their low-cost, abundant resource, stability, facile preparation and substantial catalytic activity.¹¹

Among these materials, nickel, a low-cost and earth abundant transition metal with a work function of nearly 5 eV has been considered as a potent alternative to noble-metal co-catalysts because it is already employed as a catalyst in many industrial chemical reactions.^{6,7} However, reported hydrogen generation yield of TiO_2 -Ni based heterogeneous photocatalytic water splitting systems is very low and there is scope for innovations.³⁸

Liu *et al.* prepared Ni loaded TiO_2 nanocomposite, with 6 mol% having 10–20 nm size of Ni nanoparticles around the TiO_2 surface using Wet Impregnation Method.³⁹ NiO_x nanoparticles with average size of 24 nm distantly spread over the surface of titania in the 5 wt% NiO_x -loaded TiO_2 nanocomposite.⁴⁰ (9 : 1) Ni-Zn/ TiO_2 in which Ni content is 45 wt% displayed Ni with a diameter over 100 nm, and TiO_2 nanoparticles with an averaged diameter of 25 nm.⁴¹ Ni loaded TiO_2 thin films with Ni layer thickness of ~50 nm were fabricated by Cheng *et al.* using the atomic layer deposition (ALD) technique.⁴² $\text{NiO}/\text{Ni}/\text{TiO}_2$ sandwich-like heterojunction with Ni layer of ~0.5 nm grown by the co-precipitation technique over hydrothermally prepared TiO_2 nanocables were grown by Ren *et al.*⁴³ Most of these reports discuss about Ni nanoparticles having the larger diameters or films entirely covering the

semiconductor surfaces which may limit their application as heterogeneous photocatalyst material.

So far, many different methods, including molten-salt-mediated process,⁴⁴ precipitation,⁴⁵ solvothermal,^{46,47} sol-gel,⁴⁸ electrodeposition,⁴⁹ and chemical reduction,³⁹ have been reported for synthesis of $\text{Ni}@\text{TiO}_2$ systems.⁵⁰ In this context, electroless plating which is generally used for metallization of work-pieces at macro scale, has unexpectedly emerged as a superior wet-chemical nanofabrication alternative.²⁵

This technique, by virtue of its solution chemistry and mechanistic aspects, is capable of creating nanomaterials various shapes such as nanoparticles, nanowires, nanotubes, and ultrathin films, etc., by simply immersing suitable samples into aqueous solutions for defined amounts of time.^{27,51–56}

It offers flexibility in the choice of the substrate to be metallized and is almost independent of its chemical composition, state (solid/liquid/gas), and morphology including gas nano-bubbles, emulsified droplets, biological micro-organisms, microfluidic channels, nanoparticles, and plastics.^{54–59}

In view of this, preparation of $\text{Ni}@\text{TiO}_2$ photocatalysts was herein accomplished using the *in-house* developed electroless Ni plating bath and the effect of Ni loading percentage on the photocatalytic hydrogen generation performance has been studied. To the best of our knowledge, preparation of $\text{Ni}@\text{TiO}_2$ heterogeneous photocatalyst system using electroless method has not been reported. The electroless deposited catalyst has been found to be highly efficient for the hydrogen production.

Materials and methods

Materials

TiO_2 nanopowders were procured from Aldrich (average particle size of 20 nm). For nickel loading commercial electrochemical bath was purchased from Grauer & Weil (India) Limited. Electrochemical commercial bath consisted of cleaning solution, mild etching solution, pre-activator, activator, Ni salt solution and reducing solution. For preparation of 10% sulphuric acid solution, 98% conc. H_2SO_4 procured from SRL chemicals, India was used.

Material preparation

The detailed of bath preparation process has been mentioned in the ESI as Table T1,[†] all the solutions were prepared as per the data sheet of the manufacturer, Grauer & Weil (India) Limited. Electroless nickel loading process involves different process steps which are carried out under continuous stirring and centrifugation is followed at the end of each process step which are mentioned in the Table T2 in ESI[†] and Fig. 1 depicts all the processes involved together. In a typical process, TiO_2 nanopowder surface was sequentially cleaned using the cleaning solution (maintained at 60 °C for 10 min), mild etching solution (4 min) and acid solution (2 min). At the end of each step, water washing was undertaken followed by centrifugation. Cleaned TiO_2 nanopowder surface, was treated with pre-activator solution for 2 min. However, water rinsing was not carried out after this step.



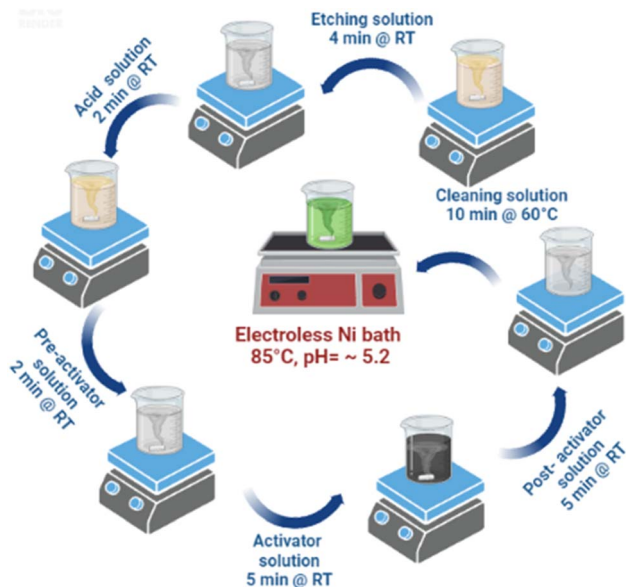


Fig. 1 Electroless Ni loading process schematic.

Preactivated TiO₂ nanopowder was surface activated by administering it to activator and post activator solutions for 5 min each followed by water rinse. Subsequently, surface activated TiO₂ (Fig. 2) nanopowder was subjected to Ni loading by transferring it to Ni bath maintained at the temperature of 85–90 °C and pH ~ 5.2, for 15 min. For varying Ni loading, surface activated TiO₂ nanopowders were treated with electroless Ni baths of various concentration and the samples, thus prepared, were used for photocatalytic water splitting application (Table 1).

Characterization techniques

Powder X-ray diffraction patterns of the Ni@TiO₂ nanopowders (XRD, Rigaku MiniFlex 600) were recorded using a Cu-K α radiation source. X-ray photoelectron spectroscopy (XPS) was conducted using PHI Versa Probe XPS. ICP-OES measurements were done using Spectroblue, Amtek. For this study, 200 mg of sample was dissolved in 4 ml con. HNO₃ and 1 ml of 30% Hydrogen Peroxide and digested in microwave digester, diluted up to 50 ml and filtered solution was run through the calibration curve. Raman spectra were measured on a Renishaw InVia Raman microscope equipped with a 532 nm laser. Diffuse reflectance UV-visible absorbance spectra (UV-DRS) were obtained at room temperature in the range of 200–800 nm using

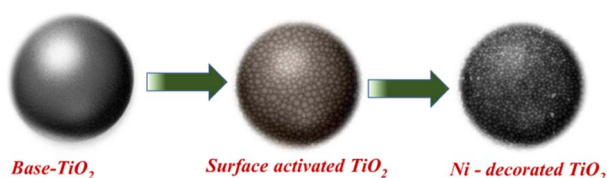


Fig. 2 Ni decoration of TiO₂ surface activation followed by electroless deposition method.

the Shimadzu UV-vis-NIR spectrophotometer (Model UV-3600). The photoluminescence emission spectra of prepared powders were carried out by using Shimadzu (RF5301PC) spectrofluorometer at an excitation wavelength 350 nm.

Fourier transform infrared (FTIR) spectroscopy measurements were carried out with a Jasco FTIR-6100 spectrometer over a range of 400–4000 cm⁻¹. Field emission scanning electron microscopy (FESEM, Hitachi, Japan with Model S-4800) and field emission transmission electron microscopy (FETEM by JEOL; JEM-2200FS) techniques were used to perform the morphological and microstructural analysis. For typical FETEM analysis, the test sample was carefully prepared by dispersing the sample powder in de-ionized water and drop of the dispersion was then transferred to carbon coated grid. In order to acquire high imaging and spatial resolution with chemical mapping of the material, out Scanning Transmission Electron Microscopy (STEM) in bright field (BF) mode equipped with energy dispersive X-ray spectroscopy (EDS) coupled elemental mapping by using JEOL, JEM2200FS equipment operated at 200 kV with spherical aberration corrector was carried out. The porosity and surface area of the samples were examined using Brunauer–Emmett–Teller analysis (BET: Quantachrome NOVA touch LX1).

Photoelectrochemical study

Incident photon-to-current conversion efficiency (IPCE) for the prepared pristine TiO₂, 0.1% Ni@TiO₂ and 0.5% Ni@TiO₂ nanopowders were measured in the wavelength region of 350–600 nm (PV Measurement Inc., USA) where a standard tungsten-halogen lamp as monochromatic light source with a broadband bias light for ~1 sun light intensity was used. The measurements related to electrochemical impedance spectroscopy (EIS) were undertaken on a CH 660C electrochemical analyzer (CH Instruments, Shanghai, China) in a two-electrode configuration where the photoanode comprising the prepared nanopowders and a platinum wire were used as working and counter electrodes respectively. The transport properties of the electrons were measured using electrochemical impedance spectroscopy (EIS) in the frequency range of 10⁻² to 10⁵ Hz at an alternative signal of 10 mV. The study on transient current–time profile for the prepared pristine TiO₂, 0.1% Ni@TiO₂ and 0.5% Ni@TiO₂ nanopowders was carried out using a Kiethley Source Measure Unit (Model 2400) under the illumination of a 1000 W xenon lamp (Oriol 91193). The homogeneity of light intensity over an 8 × 8 in² area was confirmed by calibrating it under 1 sun light intensity (AM 1.5G, 100 mW cm⁻²) with a Si solar cell.

Photocatalytic study

Photocatalytic hydrogen generation study of prepared Ni@TiO₂ nanopowders was performed using water splitting technique by following previously reported procedure.⁶⁰ For this experiment, *in-house* designed 100 ml capacity quartz glass reactor was employed which was sealed with the septum for collecting the evolved H₂ with the help of a gas tight syringe. This water splitting mediated evolved hydrogen can then be applied to gas chromatogram (Shimadzu: Model GC 2014) for quantitatively



Table 1 Electroless Ni bath composition for variable Ni% loading over TiO₂ nanoparticles

S. no.	Sample code (wt%)	Nickel salt solution (ml)	Reducing agent solution (ml)	Theoretical% Ni loading concentration
1	Pristine TiO ₂	0	0	0
2	0.05% Ni@TiO ₂	0.1	0.1875	0.05
3	0.1% Ni@TiO ₂	0.2	0.5740	0.1
4	0.2% Ni@TiO ₂	0.4	1.1480	0.2
5	0.3% Ni@TiO ₂	0.6	1.7120	0.3
6	0.4% Ni@TiO ₂	0.8	2.2960	0.4
7	0.5% Ni@TiO ₂	1	2.870	0.5

analysing its production. The main component of this photocatalytic water splitting set up is mercury vapor lamp (400 W) as the light source fitted with continuous water circulation condenser. Such condenser absorbed the IR radiation and minimized the heating effect. For studying the photocatalytic activity of pristine TiO₂ and as synthesized Ni@TiO₂ nanoparticles, 20 mg of sample was mixed with 25 ml of 20% methanol–water mixture in the quartz reactor and was kept under continuous stirring. Conventionally, Pt is added as the co-catalyst in a photocatalytic water splitting process. However, in the present case, Ni itself worked as co-catalyst and hence Pt was not added. The dissolved gases, if any, were removed by Ar gas purging (for 2 min). The reactor was kept in photocatalytic reactor set up under mercury vapor lamp irradiation and the evolved/produced hydrogen gas was collected at an interval of 60 min by means of a 5 ml capacity gas fitted syringe and finally hydrogen production was enumerated with the help of fitted standard curve data.

Result and discussion

Structural study by XRD

X-ray diffraction patterns of TiO₂ and Ni@TiO₂ powders are presented in Fig. 3. The diffractograms of all the samples exhibited tetragonal crystal structure with coexistence of anatase and rutile polymorphic phases (JCPDS card no. 02-22-1272 and 02-22-1276). The ratio of anatase to rutile phase calculated by using Spurr's formula was found to be 81 : 19.⁶¹ The diffraction peaks present at 2θ values of 25.3, 36.7, 37.8, 38.7, 48.09, 53.74, 55.05, 62.19 and 75.15° correspond to (101), (103), (004), (112), (200), (105), (211), (213) and (215) planes of TiO₂ anatase phase respectively. The diffraction peaks observed at 2θ values of 27.39, 36.05, 41.35, 54.18, 56.78, 62.69 and 68.96° are ascribable to (110), (101), (111), (211), (220), (002) and (301) planes of TiO₂ rutile phase respectively.

No additional peaks belonging to metallic nickel was observed in Ni@TiO₂ samples. This may be because of low concentration of nickel as well as electroless deposition which generally gives amorphous coating. Most of the researchers did not get Ni phase in their X-ray diffraction study of Ni@TiO₂ and hence validated by XPS.^{40,43,62,63}

X-ray photoelectron spectroscopy study

The confirmation of elemental composition as well as chemical state of 0.1% Ni loaded TiO₂ nanopowder was carried out using

X-ray photoelectron spectroscopy (XPS). The wide scan survey spectrum validated the presence of Ti, O, and Ni that are the three main elements present in the prepared samples (Fig. 4a). The peaks attributable to Ti 2p_{3/2} and Ti 2p_{1/2} were found at 458.8 eV and 459.0 eV, and at 464.5 eV and 464.7 eV, respectively (Fig. 4b).^{41,50} The binding energy difference between Ti 2p_{1/2} and Ti 2p_{3/2} was 5.68 eV, attributable to characteristic Ti–O bond of TiO₂.⁵⁰ The O 1s XPS spectra of 0.1% Ni loaded TiO₂ nanoparticles was shown in Fig. 4c which revealed their typical peak around 530.1 eV which was assigned to the lattice oxygen of the Ti–O species. Another peak at 532.5 eV related to the hydroxyl groups adsorbed on the sites of surface oxygen vacancies of the Ni@TiO₂ was noticed.

The XPS signal of Ni 2p peak at the binding energy of 851.83 eV (Fig. 4d) is associated with metallic Ni loaded on TiO₂

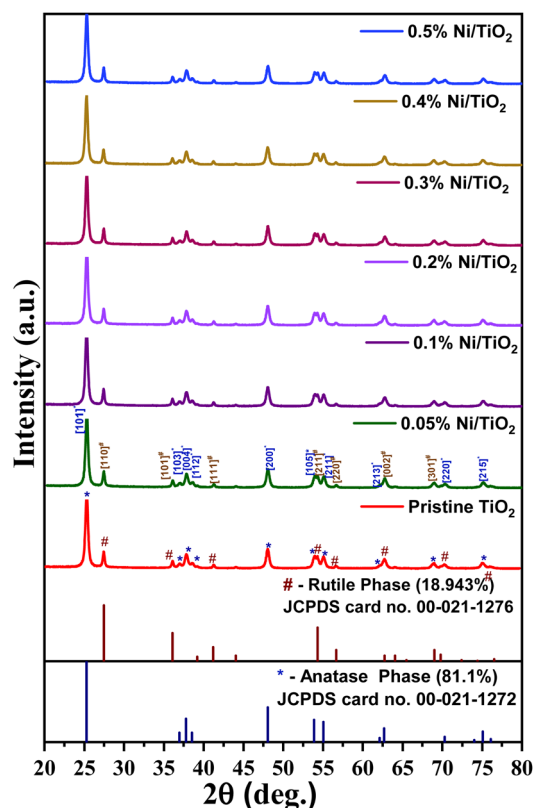


Fig. 3 X-ray diffraction patterns of pristine TiO₂ and Ni@TiO₂ powders.



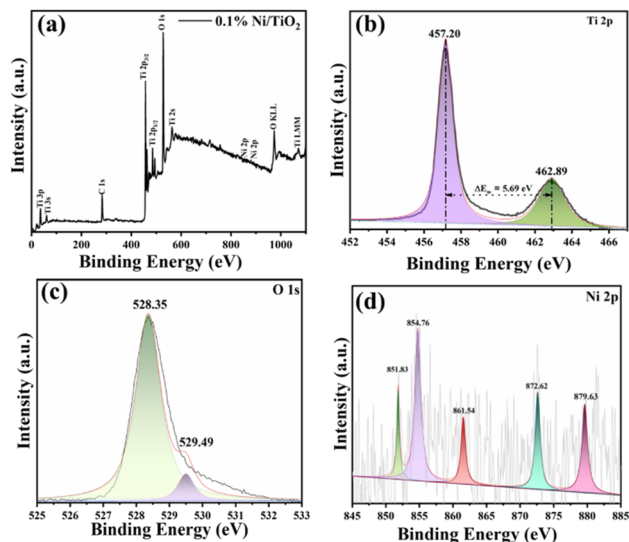


Fig. 4 XPS spectra of 0.1% Ni@TiO₂ powder corresponding to (a) survey scan, and deconvoluted high resolution scans corresponding to elements (b) Ti 2p, (c) O 1s and (d) Ni 2p.

surface which is consistent with other available reports.^{40,41} The Ni 2p XPS spectrum exhibited additional peaks at 854.76 and 872.62 eV (Fig. 4d) ascribable to the Ni²⁺ (2p_{3/2} and 2p_{1/2}) of Ni(OH)₂/NiO, their respective satellite peaks at 861.54 and 879.63 eV were observed.^{50,64} Thus, coexistence of metallic Ni and Ni(OH)₂/NiO, is observed in XPS spectra. This coexistence of metallic Ni and Ni(OH)₂/NiO is mutually beneficial. The defects in TiO₂ create an electron donor *via* captivation of Ni²⁺, generating the Ni–O bonds, which closely fix metallic Ni nanoparticles on the TiO₂ surface.⁵⁰

ICP-OES study

ICP-OES studies of Ni@TiO₂ nanopowders are presented in Table 2 which depicts that the observed wt% loading of Ni is consistent with our theoretical calculations carried out while performing the Ni loading experiments.

Raman study

According to the factor group analysis, the six different modes of anatase TiO₂, namely 1A_{1g}, 2B_{1g} and 3E_g are the Raman active modes having the following representation (1A_{1g} + 2B_{1g} + 3E_g)

Table 2 ICP-OES study results for Ni@TiO₂ nanopowders

S. no.	Ni weight% value	
	Theoretical	Observed
1	0.05% Ni@TiO ₂	0.0512
2	0.1% Ni@TiO ₂	0.0984
3	0.2% Ni@TiO ₂	0.1992
4	0.3% Ni@TiO ₂	0.2986
5	0.4% Ni@TiO ₂	0.4013
6	0.5% Ni@TiO ₂	0.4927

Table 3 Raman vibrational modes of anatase and rutile phases of TiO₂ nanoparticles

S. no.	Reported vibrational modes (cm ⁻¹)		Observed modes (cm ⁻¹)
	Anatase phase	Rutile phase	
1	144 (E _g)	144 (B _{1g})	142
2	199 (E _g)	—	197
3	399 (B _{1g})	—	395
4	—	448 (E _g)	447
5	515 (A _{1g} + B _{1g})	—	517
6	—	612 (A _{1g})	613
7	640 (E _g)	—	637
8	796 (first overtone of B _{1g})	—	793

and their reported vibrational peak positions are given in Table 3.⁶⁵ Raman spectra of the Ni@TiO₂ are shown in Fig. 5. Raman vibrational modes occurred at frequencies of 142 (E_g), 197 (E_g), 395 (B_{1g}), 516 (A_{1g} + B_{1g}), 637 (E_g) and 793 (first overtone of B_{1g}) cm⁻¹ corroborated the presence of anatase crystalline phase (Fig. 5a). This E_g peak was assigned to the symmetric bending vibration of O–Ti–O in TiO₂ frame. In case of Ni doping, it is reported that vibrational mode at 141 cm⁻¹ of

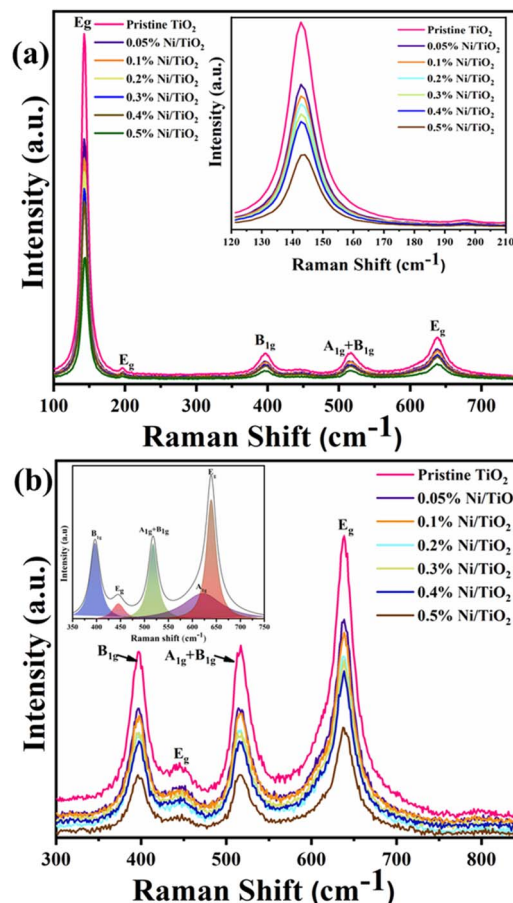


Fig. 5 Raman spectra of pristine TiO₂ and Ni@TiO₂ powders for (a) major peaks depiction (inset: enlarged image of peak at 142 cm⁻¹ due to E_g mode) and (b) major peaks in 300 to 850 cm⁻¹ range (inset: deconvoluted peaks).

Ni@TiO₂ samples showed an appreciable shift toward higher frequencies (from 143.2 to 145.0 cm⁻¹) by increasing the nickel content in the photocatalyst. However, in our samples nickel loading/decoration rather than doping is carried out, hence, noticeable shift is not observed (inset of Fig. 5a).⁶⁵

Gradual decrease in the intensity of the peaks is noticed with increase in Ni loading concentration. Such quenching may be attributable to the scattering of incident radiation by the Ni on surface of TiO₂ nanoparticles. Ni does not show any peaks in the Raman spectrum as Ni, a face-centred cubic (FCC) metal, has a single atom primitive unit cell and does not show any polarizability change due to the interaction between the electric field of the monochromatic light and dipole moment within the material.⁶⁶

Presence of rutile phase in the sample is confirmed by observed vibrational modes assigned at 142 (B_{1g}), 447 (E_g) and 613 (A_{1g}) cm⁻¹ (Fig. 5b). The shape of the band centred at 637 cm⁻¹ indicates that there could be a shoulder to this band at the lower frequency side which is further confirmed by peak deconvolution (inset of Fig. 5b) using Lorentzian curve fitting.^{63,67–69} The Raman study clearly reveals the presence of anatase and rutile TiO₂ phases.

UV DRS and photoluminescence study

Investigation of the band gap energies of pristine TiO₂ and Ni@TiO₂ nanopowders was executed using UV-DRS technique

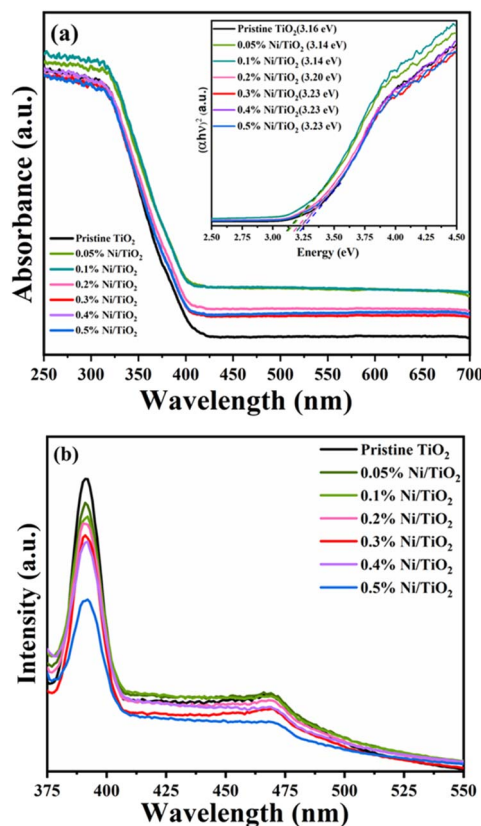


Fig. 6 (a) UV-DRS spectra (inset: Tauc plot) and (b) PL spectra of pristine TiO₂ and Ni@TiO₂ nanopowders.

and the results are shown in Fig. 6a. When the surface of TiO₂ nanopowder is decorated with Ni using electroless coating method, the absorption edges of Ni@TiO₂ samples shift towards longer wavelength and a bathochromic shift (red shift) was observed which is also reported by other investigators.^{70–72} Red shifted absorption edge was perceived as an effect of interconnectivity between the d electrons of Ni²⁺ and the electrons availed from O²⁻ and Ti⁴⁺.

Remarkably, for the pristine TiO₂ nanopowder the edge absorbance value was observed to be at 380 nm, which increased significantly to 394, 392 nm for 0.05 and 0.1% Ni@TiO₂ nanopowders and then decreased slightly to 387, 382, 382 and 382 nm, for 0.2, 0.3, 0.4 and 0.5% Ni@TiO₂ nanopowders, respectively. Such slight decrease in the absorbance edge at higher Ni loading concentrations may be attributable to excessive interaction d-electrons of Ni²⁺ and the sp-d exchanges taking place among the electrons in the conduction band of TiO₂.⁷³ Nevertheless, the band gap energy of pristine TiO₂ and 0.5, 0.1, 0.2, 0.3, 0.4 and 0.5% Ni@TiO₂ nanopowders was computed to be 3.26, 3.16, 3.14, 3.20, 3.23, 3.23 and 3.23 eV, respectively by implementing Tauc plot which revealed slight red shift (inset of Fig. 5a).

Photoelectronic features of pristine TiO₂ and Ni@TiO₂ was reported using photoluminescence spectra and the range used is 400–800 nm. Wavelength of 350 nm sweetens well to cause the excitation of electrons suitable to understand the recombination of holes and electrons. Numerous concurrent processes occur leading to recombination/reunification of electrons and holes after their excitation by photon which are dominated by electronic stoichiometry and crystal structure.⁷³ In Fig. 6b, the first band observed is at 391 nm (UV region) followed by a low intensity band around 470 nm (visible blue-green emission region) in all the samples. The first band is attributable to the band gap transition or the band edge emission of the host TiO₂. The emission band at 470 nm can be ascribable to self-trapped excitons, oxygen vacancies, surface defects, *etc.* The blue-green emission band at 470 nm originated from the charge transfer from Ti³⁺ to oxygen anion in [TiO₆]⁸⁻ complex hinting at their intrinsic state nature as against the surface state.^{72–74}

Ni²⁺ loading concentration on the surface of TiO₂ nanopowder also plays a vital role as quencher of PL peak intensity.⁷⁵ When the surface TiO₂ nanopowder is decorated with nickel, it creates an epicentre which is non-radiative in nature and prevents aggressive recombination of e⁻/h⁺ pair. This phenomenon was also observed in the PL spectra of the present work (Fig. 6b) where decrease in the PL peak intensity was noted with increase of Ni loading percentage responsible for an effective charge separation and an increase of carrier mobility as compared to the pristine TiO₂ sample.^{71,75,76} In case of samples prepared with Ni loading of 0.1 and 0.2 wt%, through the intensity of peak due to the band gap transition is decreased little bit as compared to pristine TiO₂, the intensity of peak at 470 nm due to self-trapped excitons, oxygen vacancies, surface defects, *etc.* decreased to a more extent, which may indicate interaction d electrons of Ni²⁺ and the sp-d exchanges dominate the electron-hole decay process taking place among the electrons in the conduction band of TiO₂.

FTIR study

FTIR analysis was executed to survey the characteristic vibration bands of Ni@TiO₂ catalysts and their spectra in the wavenumber range 400–4000 cm^{−1} are presented in Fig. 7. In the range of 400–800 cm^{−1}, characteristic vibration bands belonging to metal–oxygen bonds were reported.⁷⁰

From the spectra, absorption band observed in the range of 1000–1700 cm^{−1} is designated to water molecules adsorbed on the surface of nanostructure (H–O–H bending: 1639 cm^{−1}) and Ti–O–Ti stretching vibration peak at 1116 cm^{−1}.

FESEM analysis

The nanoscale morphology and shapes of pristine TiO₂ and 0.05–0.5% Ni@TiO₂ powders were examined by field emission scanning electron microscopy (Fig. 8). FESEM images of pristine TiO₂ nanopowder show nanoparticles having spherical morphology with particle size in the range of 20–30 nm (Fig. 8a and b). After electroless Ni loading on TiO₂ nanoparticles, slight increase in the particle size *i.e.* 35 nm was noted (Fig. 8c–l and ESI Fig. S2†).^{50,72}

Microstructural study by FETEM

FETEM imaging

FETEM images for 0.1% Ni loaded TiO₂ nanopowders are shown in Fig. 9. FETEM images at low and intermediate magnification (Fig. 9a and b) display hexagonal and cubical faceted morphologies having sharp-edged geometries. The particles are found to have an average size in the range of 20–30 nm. Loading of TiO₂ sample by Ni was found to occur by two ways as seen from the high magnification images (Fig. 9c–e). Ni nanofilm were found to get intermittently deposited over TiO₂ nanoparticles surface (shown by the yellow colour bordered areas in Fig. 9c and d). The width of this film was found to be in the range of 1–2 nm. Secondly, Ni nanoclusters of size around

2 nm were also observed over the surface of TiO₂ nanoparticles (as indicated by the dotted circle in Fig. 9e). The analysis of lattice fringes in Fig. 9b–e reveal presence of three types of materials. Majority of the particles displayed local single crystalline nature with each particle having a different lattice orientation. For TiO₂ nanoparticles, fringes with lattice spacing of 3.50, 2.29 and 1.91 Å belonging to (101), (004), (200) planes, respectively, corresponding to the anatase phase and 3.35 and 1.70 Å with planes for (110) and (211) corroborating the presence of rutile phase were noticed.⁷⁷ The presence of nickel was ascertained by lattice spacing fringes with *d*-value of 1.98 Å with (111) plane.⁷⁸ The nanocrystalline nature of the samples through selected area electron diffraction (SAED) patterns (Fig. 7f) was evinced by presence of ring like patterns that are not continuous and display regular bright spots.⁷⁷ Confirmation of such morphological features due to Ni loading was carried out by obtaining more such FETEM images as displayed in ESI Fig. S4.† The SAED patterns further substantiated presence of anatase and rutile phases TiO₂ when *d*-values from the corresponding rings were calculated and matched with XRD database. The presence of (101), (103), (004), (200), (105) and (110), (211) planes for anatase and rutile phases of TiO₂ respectively and (111) plane for Ni were observed. For sake of comparison, FETEM images of 0.5% Ni@TiO₂ nanopowder sample are shown in ESI Fig. S5† which also revealed the loading of TiO₂ nanopowders by Ni.

FETEM-STEM-EDS analysis of 0.1 wt% Ni@TiO₂ photocatalyst

The semi-quantitative qualification of elements present in the 0.1 wt% Ni@TiO₂ sample was ascertained using the energy dispersive X-ray spectroscopy (EDS) analysis in scanning transmission electron microscopy (STEM) mode. Ni was loaded over TiO₂ nanoparticles in weight-by-weight manner. The pertinent FETEM-EDS spectrum for 0.1 wt% Ni@TiO₂ sample with tabulated quantitative data is presented in Fig. 10a and its inset. The EDS spectrum of 0.1 Ni@TiO₂ catalyst revealed the presence of Ti, O and Ni and disclosed the presence of 65.24 wt% of titanium, 34.68 wt% of oxygen and 0.08 wt% of Ni.

This weight percentage of Ni is close to the calculated value and it is obvious that the XRD pattern did not illustrate any Ni peaks. Thus, EDS and XPS analysis data agreed well with each other (Fig. 4). EDS-elemental mapping images of 0.1 Ni/TiO₂ sample in STEM mode are shown in Fig. 10. The electron image (given in inset of Fig. 10a) and elemental mapping images ascribable to Ti and O (Fig. 10c and d, respectively) correlated well and overlapped with elemental mapping images for Ni also (Fig. 10e) and confirmed the surface loading of Ni over TiO₂ nanoparticles. Higher intensity of the colours allocated to Ti and O as compared to Ni was noticed which was tangible as very low amount of nickel was used for the surface loading of TiO₂. FETEM images were in tune with FESEM images.

BET surface area analysis

Fig. 11 displayed the N₂ adsorption–desorption isotherms of pristine TiO₂ and Ni–TiO₂ composites with varying doses of nickel loading from 0.05 to 0.5 wt%. Both pristine TiO₂ and

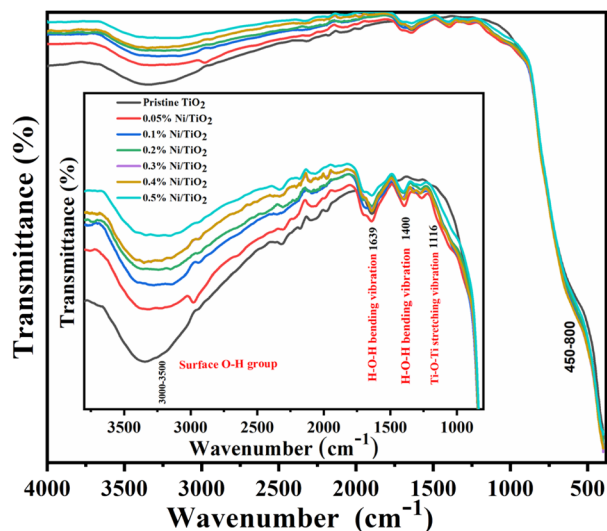


Fig. 7 FTIR spectra of pristine TiO₂ and Ni@TiO₂ nanopowders (inset: enlarged region in 1000–4000 cm^{−1} range).



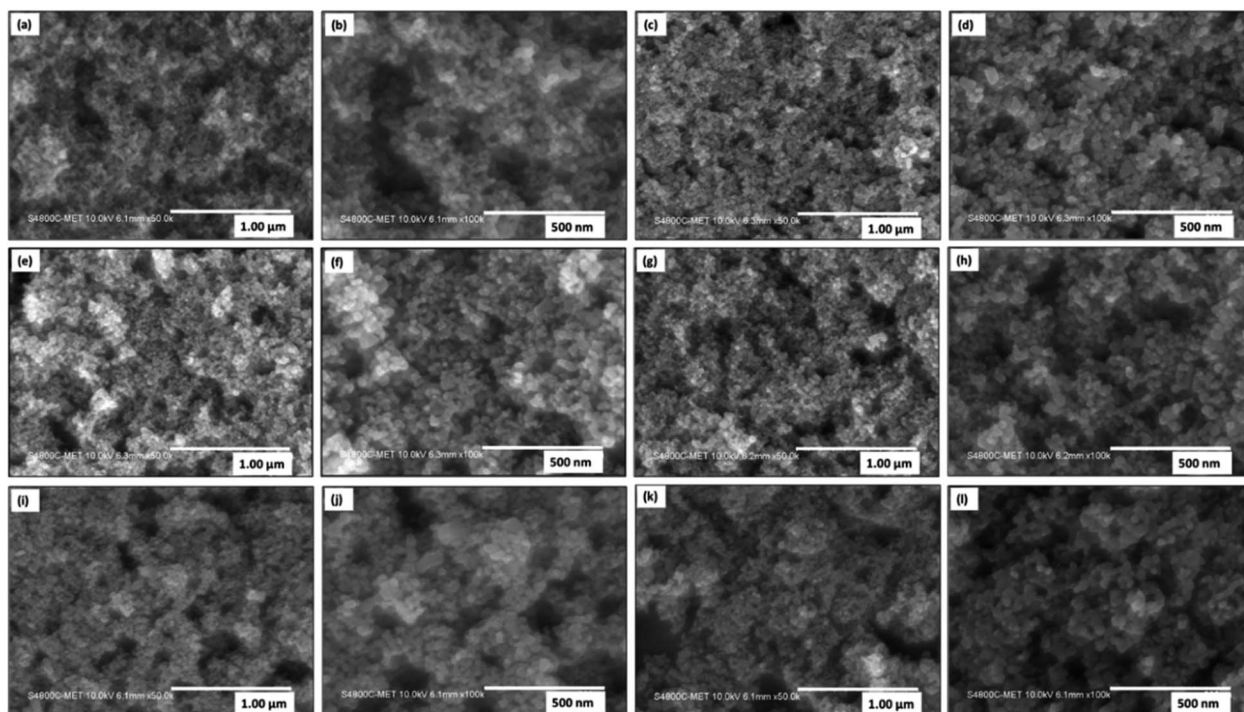


Fig. 8 FESEM images of (a and b) pristine TiO₂ and Ni@TiO₂ nanopowders with respective Ni wt% loading of (c and d) 0.05, (e and f) 0.1, (g and h) 0.2, (i and j) 0.3 at (k and l) 0.4 at low and high magnification respectively.

Ni@TiO₂ composites revealed type IV nitrogen adsorption-desorption isotherms possessing type H₃ hysteresis loops. Table 4 summarized the specific surface area, total pore volume and BJH

pore sizes of the as-prepared TiO₂ and Ni@TiO₂ photocatalyst samples. Till 0.1 wt% Ni loading, the surface area of Ni@TiO₂ nanopowders was found to increase to 61.54 m² g⁻¹ from 45.72

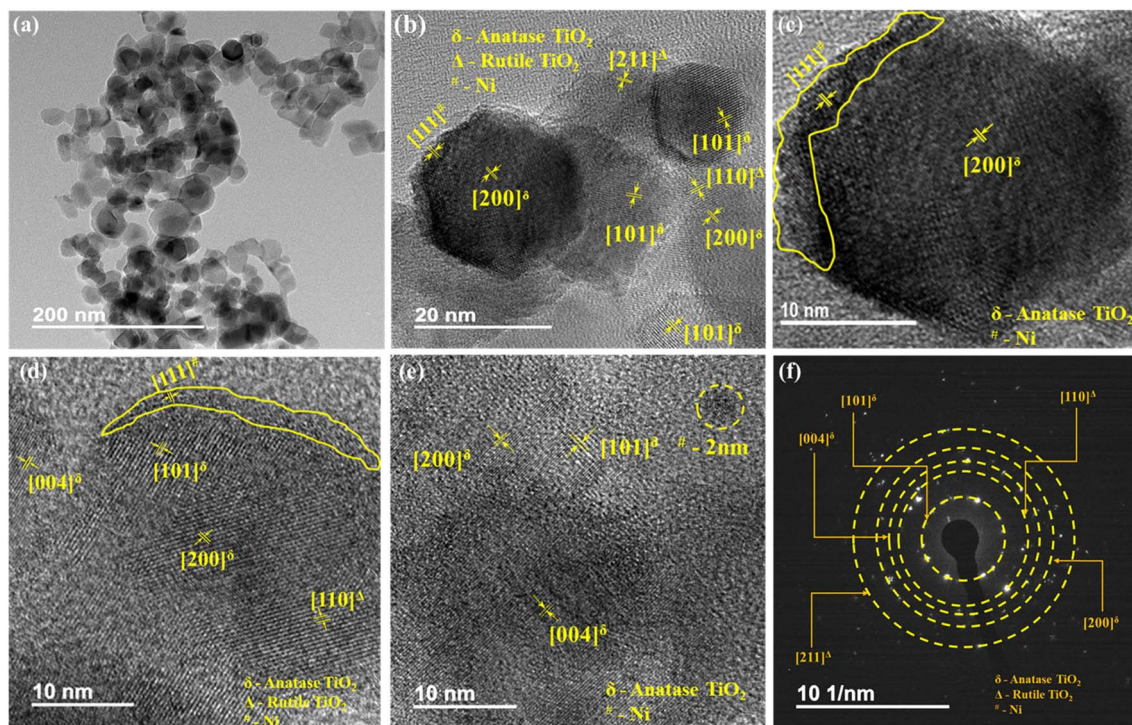


Fig. 9 FETEM images of 0.1% Ni@TiO₂ powder at (a) low magnification and their HRTEM images (b–f) the corresponding SAED pattern.



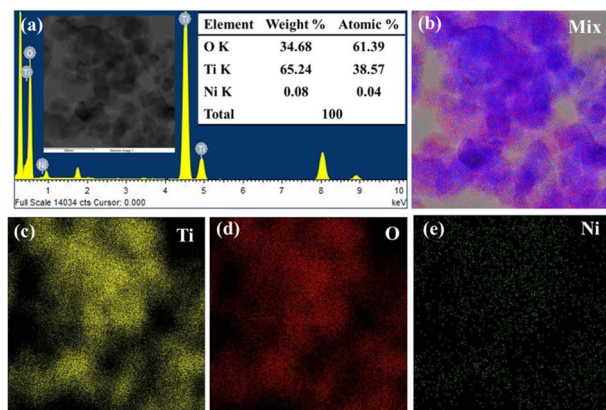


Fig. 10 FETEM-STEM-EDS elemental mapping images of 0.1% Ni@TiO₂ nanopowders: (a) EDS spectra (inset: electron image of selected region and its quantitative EDS data) and its elemental mapping images for (b) elemental mix, (c) Ti, (d) O and (e) Ni.

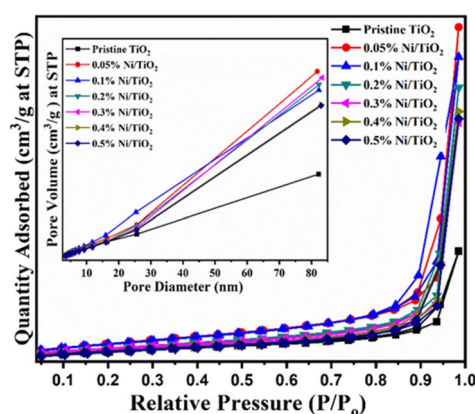


Fig. 11 BET surface area graphs of pristine TiO₂ and Ni@TiO₂ nanopowders (inset: plot of pore diameter vs. pore volume).

m² g⁻¹ for pristine TiO₂. Further increasing the Ni impregnation on TiO₂ surface above 0.1%, gradual reduction in the BET surface area was observed. It is postulated that when Ni loading amount is small (0.05 and 0.1 wt%), occupation of nucleation sites by Ni²⁺ species on TiO₂ surface leads to generation of Ni dots. As per TEM images the Ni coating is observed on the particles which might be

amorphous after aggregation of Ni dots. At higher concentration electroless nickel plating is intense which might be blocking the surface of TiO₂ which is responsible for lowering the surface area.^{60,79}

Photoelectrochemical study

IPCE study. The IPCE results of pristine and Ni@TiO₂ nanoparticles are shown in Fig. 12a. TiO₂ is known for its strong absorption of ultraviolet (UV) light, primarily in the range of 300 to 400 nanometres (nm). Consequently, the IPCE spectrum of pristine TiO₂ nanopowder showed high efficiency (with a maximum of 14% at 350 nm) in the UV range, indicating its excellent photoconversion capability in this region. The loading of Ni into TiO₂ can enhance its photocatalytic performance by modifying the band structure, improving charge carrier separation and transport, and introducing additional surface states or reaction sites. These effects can lead to an increase in the IPCE, however, 0.1% Ni@TiO₂ nanopowder exhibited better (27.21% at 350 nm) IPCE than 0.5% Ni@TiO₂ nanopowder (21.14% at 350 nm). The IPCE spectrum hints about the ability of a semiconductor in converting incident photons into electrical current across a range of wavelengths and improves the understanding of their photocatalytic or photoelectrochemical properties.⁸⁰ Herein, the IPCE results indicated that 0.1% Ni@TiO₂ nanopowder has better charge carrier separation and transport and IPCE was extended to the visible region of the solar spectrum.

Transient current–time profile. The transient current–time curves of the pristine TiO₂, 0.1% Ni/TiO₂ and 0.5% Ni/TiO₂ nanopowders are given in Fig. 12b for providing the valuable information about their electrochemical performance. The photocurrent densities of pristine TiO₂, 0.1% Ni@TiO₂ and 0.5% Ni@TiO₂ nanopowders were 15.22, 25.43 and 31.20 μA cm⁻² respectively. 0.1% Ni loaded TiO₂ nanopowder showed better photocurrent density than that of pristine and 0.5% Ni loaded TiO₂ nanopowders. The presence of nano Ni loading on TiO₂ surfaces introduces additional electrochemical reaction pathways or active sites, leading to an increase in the overall current response in terms of transient current density. In case of 0.1% Ni/TiO₂ nanopowder, the distribution of Ni intermittent films and nanoclusters on the TiO₂ surface was relatively sparse, allowing for better access to the active sites by the scavenger

Table 4 BET surface area, total pore volume, BJH pore size, H₂ generation and apparent quantum efficiency (AQE) for pristine TiO₂ and Ni@TiO₂ nanopowders

Samples	BET surface area (m ² g ⁻¹)	Total pore volume (cm ³ g ⁻¹)	BJH pore size (nm)	H ₂ generation (μmol g ⁻¹ h ⁻¹)	AQE ^a (%)
Pristine TiO ₂	45.7	0.47359	3.37834	470	3.04
0.05% Ni@TiO ₂	58.3	0.38659	3.36268	987	6.40
0.1% Ni@TiO ₂	61.5	0.2194	3.35446	1600	10.38
0.2% Ni@TiO ₂	52.6	0.39147	3.36362	1141	7.40
0.3% Ni@TiO ₂	49.2	0.42826	3.36568	1106	7.175
0.4% Ni@TiO ₂	47.8	0.43754	3.36374	1103	7.156
0.5% Ni@TiO ₂	46.6	0.45623	3.36992	997	6.468

^a AQE calculated for per gram of sample.



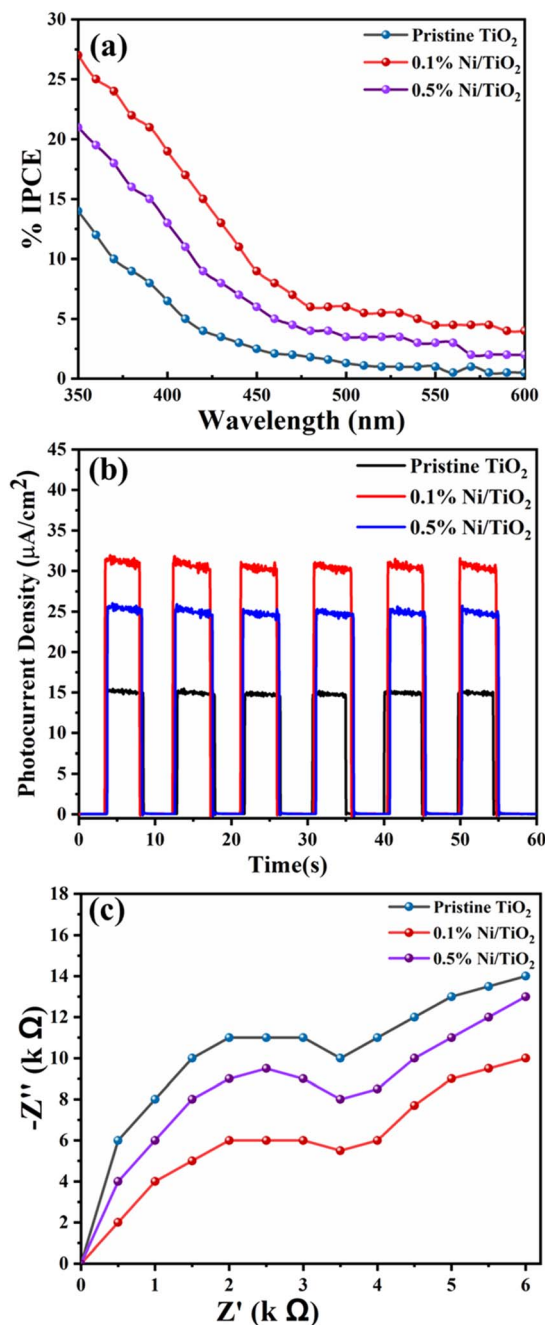


Fig. 12 Photoelectrochemical study of Ni@TiO₂ nanopowders. (a) IPCE vs. wavelength plot, (b) transient current–time profile and (c) Nyquist plot.

solution leading to more efficient charge transfer processes and a good photocurrent response in the transient current–time curve.⁴³ The observed PEC and IPCE results augmented well with the observed PL spectroscopy results.

EIS study. The Nyquist plots of pristine TiO₂, 0.1% Ni@TiO₂ and 0.5% Ni@TiO₂ nanopowders are shown in Fig. 13c. The Nyquist plots generally exhibit a semicircular arc representing the charge transfer resistance at the electrode/electrolyte interface and the efficacy photogenerated electron–hole pairs separation that is associated with the electrochemical reaction

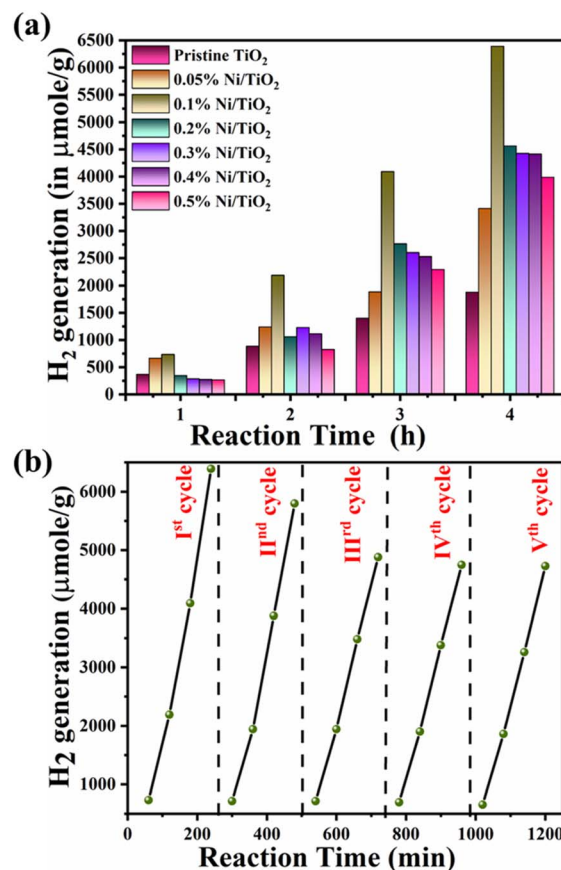


Fig. 13 (a) H₂ generation performance of pristine TiO₂ and Ni@TiO₂ nanopowders and (b) recyclability study for 0.1% Ni@TiO₂ nanopowder.

occurring on the TiO₂ surface and a linear plot associated with the diffusion region.^{43,80} Ni loading over TiO₂ surface was found to decrease the charge transfer resistance (R_{ct}) in comparison to pristine TiO₂ nanopowders as indicated by a smaller semi-circular arc of the Nyquist plot in Fig. 12C. The lower charge transfer resistance indicated improved charge transfer kinetics and enhanced electrochemical activity in Ni-loaded TiO₂. 0.1% Ni@TiO₂ nanopowder showed the lowest charge transfer resistance due to favourable electronic interactions at the Ni–TiO₂ interface, optimal active sites, and band structure modification. These factors contributed to efficient charge transfer and improved electrochemical performance. In nutshell, the photo-electrochemical and allied studies revealed that 0.1% Ni@TiO₂ nanopowders exhibited the least charge transfer resistance and optimal photocurrent density as well as IPCE values revealing that it is equipped with a good charge transfer interface and larger number of active sites.

Photocatalytic water splitting. The hydrogen generation ability of all *in situ* Ni decorated TiO₂ nanopowders based heterogeneous photocatalytic system was revealed to be at least more than double than that of pristine TiO₂ nanopowder (Table 4). It was observed that up to 0.1 wt% Ni loading, increase in the hydrogen generation rate was observed which was further reduced upon higher Ni loading. The maximum hydrogen generation rate



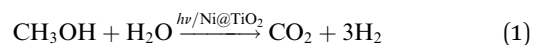
of $\sim 1600 \mu\text{mol g}^{-1} \text{h}^{-1}$ was achieved for 0.1% Ni@TiO₂, which is ~ 3.5 times higher than that of pristine TiO₂ nanopowder ($470 \mu\text{mol g}^{-1} \text{h}^{-1}$) (Fig. 13a). The optimized AQE was observed to be 10.38% at 450 nm incident light wavelength for 0.1% Ni@TiO₂ photocatalyst, attributable to efficient Ni co-catalysts on the surface activated TiO₂ nanoparticle facets leading to smoother charge separation (Table 4).⁸¹ The formulae used in the calculation of AQE are given in ESI, Section S1.†

In electroless coating method, semiconductor surface was first cleaned, activated and then metallic loading was undertaken which might be helpful for uniform decoration of Ni on TiO₂. It may be noted that Ni nanoparticles generated on TiO₂ are not just adhered to the surface by physical forces, but chemically through sp-d exchanges. Additionally, presence of nickel obliterated necessity of Pt, a commonly used co-catalyst in water splitting reactions which makes the process economical. Recyclability study of 0.1% Ni@TiO₂ photocatalyst was also carried out and the results are shown in Fig. 13b. The decrease in the photocatalytic activity from $6391 \mu\text{mol g}^{-1}$ to 5795, 4878, 4748 and $4728 \mu\text{mol g}^{-1}$ in the 2nd, 3rd, 4th and 5th cycles correspond to loss of 90.67%, 76.32%, 74.29% and 73.97% respectively than the initial photocatalytic activity. However, these losses are attributed to the material loss during the processing and washing of the catalysts after first cycle. The 20, 18 mg of catalysts are used for 1st, 2nd respectively and for 3rd cycle onwards 16 mg of catalyst was used. It showed almost similar hydrogen evolution for three cycles, ultimately revealing the good stability of the photocatalyst. FETEM images of recycled 0.1% Ni/TiO₂ nanopowder photocatalyst are given in ESI Fig. S6† which also revealed the stability of the photocatalyst by the presence of Ni over TiO₂ nanoparticles.

Mechanism of photocatalytic H₂ generation of prepared Ni@TiO₂ nanopowders. Photocatalysis process can be divided into homogeneous and heterogeneous based on the use of only catalyst and additional co-catalyst respectively. The schematic representing the mechanism of photocatalytic H₂ generation in heterogeneous scheme was presented in Fig. 14. In the water-splitting reaction, the photogenerated electrons and holes are

produced when Ni@TiO₂ nanopowders were irradiated by light.^{9,11} During this process, the migration of photoexcited electrons and holes to the surface of TiO₂ occurs, that are responsible for H⁺ reduction. For H₂ evolution, the more negative CB potential of TiO₂ than the reduction potential of water leads to generation of a swift pathway for photogenerated species for migration towards reaction sites present on its surface, which in turn, reduces the probability of recombination. The further enhancement of photocatalytic efficacy for Ni@TiO₂ nanopowders than pristine TiO₂ nanopowder might be due to the effective electron acceptor property of Ni and the Schottky barrier formation between these two materials.

In photocatalytic H₂ generation with methanol as sacrificial agent, photogenerated electrons are used to combine with protons in water to generate H₂, while the methanol molecules get oxidized by capturing excess photogenerated holes through a series of reactions finally yielding three hydrogen molecules as given in eqn (1).



Ni loaded on TiO₂ as co-catalysts, absorbs photogenerated electrons to promote the separation and transfer of interface charge carriers, but also provide efficient proton reduction centres.⁸²

It may be noted that the CB level of TiO₂ is -0.50 V above the H₂ evolution potentials and that of Ni is just -0.23 V and this potential gradient helps in transformation of photoexcited electrons from CB of TiO₂ to Ni nanoparticles which subsequently react with H⁺ ions generated by oxidation of water to form H₂ gas.

Beyond the optimized loading, the decreased in the photocatalytic activity was found. In this context, it may be noted the photocatalytic hydrogen generation results corroborate well with BET and PL spectroscopy results. BET surface area was found to increase for Ni decorated TiO₂ nanopowders than pristine TiO₂ up to 1 wt% Ni loading and then decreased gradually. Similarly, quenching in PL intensity peak and the peak due to presence of defects was noted (Fig. 5b). Both these phenomena were attributed to the density of non-radiative epicentres (causing the increase in Ni particle size as well as defect centres) which, in turn, are responsible for recombination of electron-hole pairs and ultimately reflects on the photocatalytic activity.

Conclusion

Nickel-decorated TiO₂ photocatalytic system proficient of responding to visible light was successfully synthesized by autocatalytic deposition (electroless) method. In this study, nickel loading wt% increased on the TiO₂ nanopowder surface as a function of Ni concentration in electroless bath. The existence of metallic Ni (in the form of nanocluster and intermittent films) that was uniformly infused onto the TiO₂ nanopowder surface was observed in the FETEM images which was further confirmed by EDS (and allied elemental mapping images) and

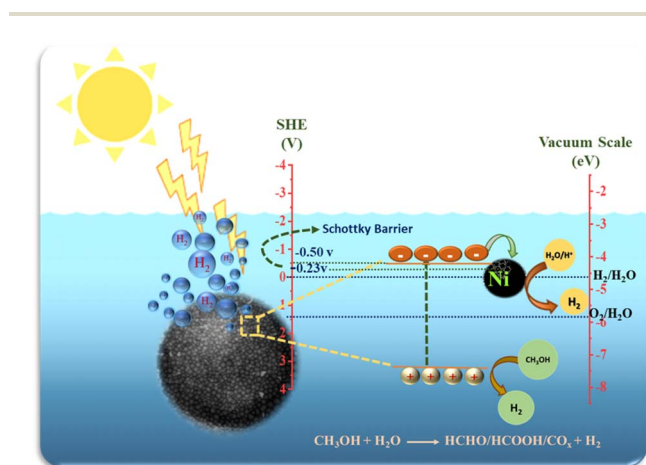


Fig. 14 Mechanism of photocatalytic H₂ generation of prepared Ni@TiO₂ nanopowders.



XPS spectroscopy techniques. Ni²⁺ loading concentration on the surface of TiO₂ nanopowder also plays a vital role as quencher of PL peak intensity and as an effective charge separator. The further enhancement of photocatalytic efficacy for Ni@TiO₂ nanopowders than pristine TiO₂ nanopowder might be due to the effective electron acceptor property of Ni and the Schottky barrier formation between these two materials. 0.1% Ni@TiO₂ nanopowder exhibited the optimized hydrogen generation rate of ~1600 μmol g⁻¹ h⁻¹ which is ~3.5 times higher as compared to pristine TiO₂ nanopowder (470 μmol g⁻¹ h⁻¹) and the photocatalyst exhibited fairly good repeatable behaviour. In nutshell, electroless-plating is an efficient technique to decorate TiO₂ nanopowder surface using nickel which can not only serve as an efficient and cost-effective heterogeneous photocatalyst but in other applications like gas sensors.

Author contributions

The experiments have been planned by B. B. K., S. B. R., S. K. K., S. J. and P. N. B. performed the experiment. The data were analysed by P. N. B., M. D. S. and S. S. A. All the authors participated in writing the manuscript under the lead of B. B. K.

Conflicts of interest

There are no conflicts to declare.

Acknowledgements

The authors are thankful to the HRD/Knowledge Management Division, Ministry of Electronics and Information Technology (MeitY) and Department of Science and Technology (DST) KIRAN Division for DST Women Scientist fellowship (DST/WOS-A/CS-14/2021) New Delhi.

References

- Y. Li and S. C. E. Tsang, *Mater. Today Sustain.*, 2020, **9**, 100032.
- S. Chen, D. Huang, P. Xu, W. Xue, L. Lei, M. Cheng, R. Wang, X. Liu and R. Deng, *J. Mater. Chem. A*, 2020, **8**, 2286–2322.
- C. Acar, I. Dincer and G. F. Naterer, *Int. J. Energy Res.*, 2016, **40**, 1449–1473.
- L. Sun, Q. Luo, Z. Dai and F. Ma, *Coord. Chem. Rev.*, 2021, **444**, 214049.
- M. Pein, N. C. Neumann, L. J. Venstrom, J. Vieten, M. Roeb and C. Sattler, *Int. J. Hydrogen Energy*, 2021, **46**, 24909–24918.
- Z. P. Ifkovits, J. M. Evans, M. C. Meier, K. M. Papadantonakis and N. S. Lewis, *Energy Environ. Sci.*, 2021, **14**, 4740–4759.
- T. Hisatomi, J. Kubota and K. Domen, *Chem. Soc. Rev.*, 2014, **43**, 7520–7535.
- T. A. H. Ratlamwala and I. Dincer, *Int. J. Hydrogen Energy*, 2014, **39**, 20744–20753.
- S. Chen, T. Takata and K. Domen, *Nat. Rev. Mater.*, 2017, **2**, 17050.
- S. Pasternak and Y. Paz, *ChemPhysChem*, 2013, **14**, 2059–2070.
- X. Liu and H. Zhuang, *Int. J. Energy Res.*, 2021, **45**, 1480–1495.
- Z. Wang, C. Li and K. Domen, *Chem. Soc. Rev.*, 2019, **48**, 2109–2125.
- T. S. Teets and D. G. Nocera, *Chem. Commun.*, 2011, **47**, 9268–9274.
- Z. Kang, H. Guo, J. Wu, X. Sun, Z. Zhang, Q. Liao, S. Zhang, H. Si, P. Wu, L. Wang and Y. Zhang, *Adv. Funct. Mater.*, 2019, **29**, 1–10.
- X. Ning and G. Lu, *Nanoscale*, 2020, **12**, 1213–1223.
- Y. Wang, Y. Wu, K. Sun and Z. Mi, *Mater. Horiz.*, 2019, **6**, 1454–1462.
- N. T. Thanh Truc, N. Thi Hanh, D. T. Nguyen, H. T. Trang, V. N. Nguyen, M. N. Ha, T. D. C. Nguyen and T. D. Pham, *J. Solid State Chem.*, 2019, **269**, 361–366.
- A. Fujishima and K. Honda, *Nature*, 1972, **238**, 37–38.
- C. Karthikeyan, P. Arunachalam, K. Ramachandran, A. M. Al-Mayouf and S. Karuppuchamy, *J. Alloys Compd.*, 2020, **828**, 154281.
- M. Ismael, *J. Environ. Chem. Eng.*, 2020, **8**, 103676.
- H. Lin and C. Shih, *J. Mol. Catal. A: Chem.*, 2016, **411**, 128–137.
- K. Matsubara, M. Inoue, H. Hagiwara and T. Abe, *Appl. Catal., B*, 2019, **254**, 7–14.
- L. Yang, N. Feng, Q. Wang, Y. Chu, J. Xu and F. Deng, *Cell Rep. Phys. Sci.*, 2020, **1**, 100013.
- H. Li, W. Zhang, L. Niu, J. Wang, Z. Zuo and Y. Liu, *New J. Chem.*, 2022, **46**, 7118–7127.
- F. Muench, *ChemElectroChem*, 2021, **8**, 2993–3012.
- M. S. Abd-Elwahed, A. M. Sadoun and M. Elmahdy, *J. Mater. Res. Technol.*, 2020, **9**, 13749–13758.
- K. C. Poon, D. C. L. Tan, T. D. T. Vo, B. Khezri, H. Su, R. D. Webster and H. Sato, *J. Am. Chem. Soc.*, 2014, **136**, 5217–5220.
- Y. Zhou, S. Yang, D. Fan, J. Reilly, H. Zhang, W. Yao and J. Huang, *ACS Appl. Nano Mater.*, 2019, **2**, 1027–1032.
- Y. Yang, C. Zhou, W. Wang, W. Xiong, G. Zeng, D. Huang, C. Zhang, B. Song, W. Xue, X. Li, Z. Wang, D. He, H. Luo and Z. Ouyang, *Chem. Eng. J.*, 2021, **405**, 12654.
- M. A. Mannaa, K. F. Qasim, F. T. Alshorifi, S. M. El-Bahy and R. S. Salama, *ACS Omega*, 2021, **6**, 30386–30400.
- X. Luo, R. Li, K. P. Homewood, X. Chen and Y. Gao, *Appl. Surf. Sci.*, 2020, **505**, 144099.
- P. Qiao, J. Wu, H. Li, Y. Xu, B. Sun, L. Ren, K. Pan, L. Wang and W. Zhou, *Nanotechnology*, 2019, **30**, 125703.
- S. Jayachitra, D. Mahendiran, P. Ravi, P. Murugan and M. Sathish, *Appl. Catal., B*, 2022, **307**, 121159.
- H. She, X. Ma, K. Chen, H. Liu, J. Huang, L. Wang and Q. Wang, *J. Alloys Compd.*, 2020, **821**, 153239.
- P. Ravi, V. Navakoteswara Rao, M. V Shankar and M. Sathish, *Int. J. Hydrogen Energy*, 2020, **45**, 7517–7529.
- X. Chen, B. Sun, J. Chu, Z. Han, Y. Wang, Y. Du, X. Han and P. Xu, *ACS Appl. Mater. Interfaces*, 2022, **14**, 28945–28955.
- J. Liu, J. Ke, Y. Li, B. Liu, L. Wang, H. Xiao and S. Wang, *Appl. Catal., B*, 2018, **236**, 396–403.
- S. Fang, Z. Sun and Y. H. Hu, *ACS Catal.*, 2019, **9**, 5047–5056.
- Y. Liu, Z. Wang, W. Fan, Z. Geng and L. Feng, *Ceram. Int.*, 2014, **40**, 3887–3893.



- 40 S. Fang, Z. Sun and Y. H. Hu, *ACS Catal.*, 2019, **9**, 5047–5056.
- 41 F. Neațu, L. E. Abramiuc, M. M. Trandafir, R. F. Negrea, M. Florea, C. M. Teodorescu and S. Neațu, *ChemCatChem*, 2020, **12**, 4642–4651.
- 42 H. E. Cheng, C. H. Hung, I. S. Yu and Z. P. Yang, *Catalysts*, 2018, **8**, 440.
- 43 X. Ren, P. Gao, X. Kong, R. Jiang, P. Yang, Y. Chen, Q. Chi and B. Li, *J. Colloid Interface Sci.*, 2018, **530**, 1–8.
- 44 M. Xiao, L. Zhang, B. Luo, M. Lyu, Z. Wang, H. Huang, S. Wang, A. Du and L. Wang, *Angew. Chem.*, 2020, **132**, 7297–7301.
- 45 Z. Fu, G. Zhang, Z. Tang and H. Zhang, *Catal. Surv. Asia*, 2020, **24**, 38–58.
- 46 C. Huang, Y. Ding, C. Hao, S. Zhou, X. Wang, H. Gao, L. Zhu and J. Wu, *Chem. Eng. J.*, 2019, **378**, 122202.
- 47 A. Shukla, R. K. Singha, T. Sasaki, S. Adak, S. Bhandari, V. V. D. N. Prasad, A. Bordoloi and R. Bal, *Mol. Catal.*, 2020, **490**, 110943.
- 48 M. Pudukudy, Z. Yaakob, A. Kadier, M. S. Takriff, N. Suhaimi and M. Hassan, *Int. J. Hydrogen Energy*, 2021, **42**, 16495–16513.
- 49 K. Mech, M. Gajewska, M. Marzec and K. Szaciłowski, *Mater. Chem. Phys.*, 2020, **255**, 2–12.
- 50 H. T. Li, W. G. Zhang, L. Niu, J. Wang, Z. J. Zuo and Y. M. Liu, *New J. Chem.*, 2022, **46**, 7118–7127.
- 51 M. S. Abd-Elwahed, A. M. Sadoun and M. Elmahdy, *J. Mater. Res. Technol.*, 2020, **9**, 13749–13758.
- 52 J. Song, M. R. Kim, Y. Kim, D. Seo, K. Ha, T. E. Song, W. G. Lee, Y. Lee, K. C. Kim, C. W. Ahn and H. Han, *Nanotechnology*, 2022, **33**, 065303.
- 53 M. D. Balela and K. L. Amores, *Mater. Chem. Phys.*, 2019, **225**, 393–398.
- 54 M. Scheuerlein, F. Muench, U. Kunz, T. Hellmann, J. Hofmann and W. Ensinger, *ChemElectroChem*, 2020, **7**, 3496–3507.
- 55 T. Boettcher, S. Schaefer, M. Antoni, T. Stohr, U. Kunz, M. Dürrschnabel, L. Molina-Luna, W. Ensinger and F. Muench, *Langmuir*, 2019, **35**, 4246–4253.
- 56 X. Meng, Y. Xu, Q. Wang, X. Yang, J. Guo, X. Hu, L. Tan and Y. Chen, *Langmuir*, 2019, **35**, 9713–9720.
- 57 M. Lan, J. Cai, L. Yuan, Y. Xu and D. Zhang, *Surf. Coat. Technol.*, 2013, **216**, 152–157.
- 58 T. Tsuneyoshi, Y. Cui, H. Ishida, T. Watanabe and T. Ono, *Langmuir*, 2019, **35**, 13311–13317.
- 59 J. Xu, X. Li, Y. Zhong, J. Qi, Z. Wang, Z. Chai, W. Li, C. Jing and Y. Cheng, *Adv. Mater. Technol.*, 2018, **3**, 1800372.
- 60 N. Jawale, S. Arbu, G. Umarji, M. Shinde, B. Kale and S. Rane, *RSC Adv.*, 2023, **13**, 2418–2426.
- 61 Anita, A. K. Yadav, N. Khatun, S. Kumar, C. M. Tseng, S. Biring and S. Sen, *J. Mater. Sci.: Mater. Electron.*, 2017, **28**, 19017–19024.
- 62 N. Mukurala, S. Suman, A. Bhardwaj, K. Mokurala, S. H. Jin and A. K. Kushwaha, *Appl. Surf. Sci.*, 2021, **551**, 149377.
- 63 T. Raguram and K. S. Rajni, *J. Mater. Sci.: Mater. Electron.*, 2021, **32**, 18264–18281.
- 64 S. Biswas, H. Y. Lee, M. Prasad, A. Sharma, J. S. Yu, S. Sengupta, D. D. Pathak and A. Sinhamahapatra, *ACS Appl. Nano Mater.*, 2021, **4**, 4441–4451.
- 65 M. Balakrishnan and R. John, *J. Mater. Sci.: Mater. Electron.*, 2021, **32**, 5295–5308.
- 66 A. Y. Faid, A. O. Barnett, F. Seland and S. Sunde, *Electrochim. Acta*, 2020, **361**, 137040.
- 67 M. P. B. Vega, M. Hinojosa-Reyes, A. Hernández-Ramírez, J. L. G. Mar, V. Rodríguez-González and L. Hinojosa-Reyes, *J. Sol-Gel Sci. Technol.*, 2018, **85**, 723–731.
- 68 T. Ohsaka, F. Izumi and Y. Fujiki, *J. Raman Spectrosc.*, 1978, **7**, 321–324.
- 69 U. Balachandran and N. G. Eror, *J. Solid State Chem.*, 1982, **42**, 276–282.
- 70 F. Dönmez and N. Ayas, *Int. J. Hydrogen Energy*, 2021, **46**, 29314–29322.
- 71 J. Park, S. S. Lam, Y. K. Park, B. J. Kim, K. H. An and S. C. Jung, *Environ. Res.*, 2023, **216**(3), 114657.
- 72 T. Raguram and K. S. Rajni, *Appl. Phys. A: Mater. Sci. Process.*, 2019, **125**, 1–11.
- 73 Alamgir, W. Khan, S. Ahmad, M. Mehedi Hassan and A. H. Naqvi, *Opt. Mater.*, 2014, **38**, 278–285.
- 74 B. Choudhury and A. Choudhury, *J. Lumin.*, 2012, **132**, 178–184.
- 75 N. Liu, S. Mohajernia, N. T. Nguyen, S. Hejazi, F. Plass, A. Kahnt, T. Yokosawa, A. Osvet, E. Spiecker, D. M. Guldi and P. Schmuki, *ChemSusChem*, 2020, **13**, 4937–4944.
- 76 T. Te Wang, C. L. Chiang, Y. C. Lin, V. Srinivasadesikan, M. C. Lin and Y. G. Lin, *Appl. Surf. Sci.*, 2020, **511**, 145548.
- 77 D. B. Bankar, R. R. Hawaldar, S. S. Arbu, M. H. Moulavi, S. T. Shinde, S. P. Takle, M. D. Shinde, D. P. Amalnerkar and K. G. Kanade, *RSC Adv.*, 2019, **9**, 32735–32743.
- 78 B. H. R. Suryanto, Y. Wang, R. K. Hocking, W. Adamson and C. Zhao, *Nat. Commun.*, 2019, **10**, 1–10.
- 79 X. Luo, R. Li, K. P. Homewood, X. Chen and Y. Gao, *Appl. Surf. Sci.*, 2020, **505**, 144099.
- 80 X. Li, D. T. Wang, J. F. Chen and X. Tao, *Electrochim. Acta*, 2012, **80**, 126–132.
- 81 Y. Qi, Y. Zhao, Y. Gao, D. Li, Z. Li, F. Zhang and C. Li, *Joule*, 2018, **2**, 2393–2402.
- 82 J. Zhao, R. Shi, Z. Li, C. Zhou and T. Zhang, *Nano Sel.*, 2020, **1**, 12–29.

